In partial fulfillment of the requirements for the degree

MASTER OF PHYSICS

Option Theoretical Physics

On the topic of:

Magnetism of the Square Lattice

Presented by:
Mr. NGOMA-MANICKA
Christian Diehl

Defended in July 2024, before the panel composed of:

Dr. Guy TRAMBLY DE LAISSARDIÈRE	- **Supervisor**
Dr. Geneviève ROLLET	- **Examiner**
Prof. Dr. Andreas HONECKER	- **Examiner**

Academic Year 2023-2024

Abstract

This report presents a comprehensive study on the magnetism of a square lattice at half-filling and below, conducted at the Laboratoire de Physique Théorique et Modélisation (LPTM) in Cergy. Using the Hubbard model, we employed mean field theory to calculate the diagonal terms and Hartree-Fock approximations for the off-diagonal terms of the Hamiltonian. Calculations were primarily conducted in real space, with k-space integration added for precision. Our computations, performed at near-zero temperature (10^{-7} eV) as well as at 0.1 and 0.2 eV, spanned square lattice sizes from 6×6 to 20×20, with periodic boundary conditions. Results confirmed known theoretical outcomes, such as antiferromagnetic order at half-filling, the Néel temperature, and the inability to reach the ground state with odd-sized lattices. Our findings were consistent with those of Scholle et al., and we observed faster convergence with fewer iterations on more advanced processors. The study utilized C++ with Armadillo, OpenBLAS, and LAPACK, with data management and plotting done using Python's Matplotlib and Pandas. This work enhances our understanding of magnetic order in square lattices and provides a solid foundation for future research.

Acknowledgements

First and foremost, I want to express my deep gratitude to **God** for granting me the strength, health, and wisdom necessary to complete this internship and this report.

I sincerely thank my internship supervisor, **Dr. Guy Trambly de Laissardière**, for his valuable guidance, insightful advice, and constant support throughout this experience. I also extend my thanks to **Dr. Geneviève Rollet**, who, along with **Dr. Guy Trambly de Laissardière**, encouraged me and provided the opportunity to pursue this Master's program at the University of Cergy Pontoise. Their expertise and availability were key factors in the success of this project.

I would also like to express my appreciation to the entire faculty of the University of Cergy Pontoise for their high-quality teaching, encouragement, and commitment to our education. A special thanks to **Prof. Andreas Honecker** for his valuable advice.

A special thank you goes to my family, particularly my mother, for her unconditional love, constant encouragement, and unwavering moral support. Your presence and prayers have greatly helped me throughout this journey.

I will not forget my friends, who have been a source of motivation and comfort. A special thank you to **Léonardine** for her sincere friendship, encouragement, and invaluable help. I also want to thank the following for their encouragement and moral support: **Anne-Milka, Betina, Emna, Elsa, Esther, Gloria, Glaury, Haroon, Laura, Léa, Leslie, Lamine, Marie-Paule, Néhémie, Orlane, Pierre, Soreya, Yoldie, and Zoé**.

I also want to warmly thank all those who assisted me in proofreading my report, especially **Lamine** for his detailed feedback. Your remarks and suggestions were essential in improving the quality of this document.

Finally, I wish to thank myself for the perseverance, determination, and effort put forth throughout this journey. This experience has allowed me to grow both professionally and personally.

Thank you all.

Resumé

Cette étude se concentre sur le magnétisme d'un réseau carré au demi-remplissage et en dessous, réalisée au Laboratoire de Physique Théorique et Modélisation (LPTM) à Cergy. Le LPTM est une unité mixte de recherche de CY Cergy Paris Université et du Centre National de la Recherche Scientifique (UMR 8089), spécialisée dans la physique théorique, la physique statistique et la physique numérique. En utilisant le modèle de Hubbard, nous avons appliqué la théorie du champ moyen pour les termes diagonaux et les approximations de Hartree-Fock pour les termes hors diagonaux, avec des calculs principalement en espace réel et une intégration supplémentaire en espace k pour plus de précision. Les calculs ont été effectués à des températures quasi nulles (10^{-7} eV), 0.1 eV et 0.2 eV sur des tailles de réseau carré allant de 6×6 à 20×20, avec conditions aux bords périodiques. Nos résultats, conformes aux prédictions théoriques et aux résultats de Scholle et al., ont confirmé l'ordre antiferromagnétique au demi-remplissage, la température de Néel et la difficulté d'atteindre l'état fondamental avec des réseaux de taille impaire. Le travail a utilisé C++ avec Armadillo, OpenBLAS et LAPACK, ainsi que Matplotlib et Pandas de Python pour la gestion et la visualisation des données, fournissant des insights précieux sur l'ordre magnétique dans les réseaux carrés.

Contents

List of Figures

Chapter 1

Introduction

Magnetism in condensed matter physics is a field of great interest due to its fundamental implications and potential applications in various technological domains. The study of magnetic properties in lattice structures, particularly square lattices, provides valuable insights into the behavior of materials at the atomic level. This report delves into the investigation of magnetism in a square lattice using the Hubbard model, a widely used theoretical framework for describing electron interactions in a lattice.

This study was conducted at the Laboratoire de Physique Théorique et Modélisation (LPTM) in Cergy [8]. The LPTM is a joint research unit of CY Cergy Paris Université and the Centre National de la Recherche Scientifique (UMR 8089). The research activities at LPTM focus on theoretical physics, statistical physics, and computational physics, primarily addressing issues of order-disorder in matter, out-of-equilibrium phenomena, non-linear physics, and integrable models. The LPTM is also committed to the dissemination of knowledge through its teaching activities at CY Cergy Paris Université.

The primary goal of this research is to study the magnetism of a square lattice at half-filling and below. While it is established that the system exhibits antiferromagnetic order at half-filling, this study aims to explore the magnetic order below half-filling. We employed mean field theory to calculate the diagonal terms of the Hubbard Hamiltonian (Hartree terms) and added the Fock approximation to account for the off-diagonal terms. Nearly all calculations were performed in real space, with additional k-space integration to enhance computational precision.

A significant part of this research involved replicating and extending the results obtained by Scholle *et al.* [12]. Their work provided a foundation, and our aim was also to verify if the inclusion of k-space integration, which Scholle *et al.* did not utilize, would impact the results. This comparative analysis highlighted the robustness of our approach and the consistency of our results with existing literature. The similarity in results confirmed the reliability of our computational framework and provided confidence in our conclusions.

The computational aspect of this research involved developing a C++ code (see [9]) using Armadillo [11], OpenBLAS, and LAPACK libraries to calculate spin densities and local magnetic moments. These calculations were conducted at near-zero temperature ($10^{-7}t$, with t the hopping amplitude), $0.1t$, and $0.2t$ across an $N \times N$ superlattice of a simple square lattice, N varying from 6 to 20, with periodic boundary conditions. Our results confirmed several theoretical expectations, such as antiferromagnetic order at half-filling, the existence of the Néel temperature, and that the results are highly dependent on the parity of N. We therefore distinguish between cases with even N and odd N.

Temperature plays a pivotal role in determining the magnetic properties of materials. At half-filling, the Néel temperature marks the transition point to antiferromagnetic order. This study's identification of the Néel temperature provided critical validation of our computational methods. Furthermore, the electron density within the lattice is another crucial factor influencing magnetic order. We explored various average electron densities, focusing on scenarios at half-filling and below. The behavior of the system under these conditions provided insights into the interplay between electron interactions and magnetic properties.

One significant finding was the observation that computations on more advanced processors not only ran faster but also sometimes required fewer iterations to reach convergence. This aspect highlights the impact of computational power on the efficiency of simulations. Despite attempts to use Intel's Math Kernel Library (MKL) for further speed improvements, these efforts were not successful.

Python, utilizing Matplotlib and Pandas, was extensively used for plotting and managing data. The visual representations facilitated a comprehensive analysis of the magnetic orders observed under different conditions. These tools enabled us to manage large datasets efficiently and create clear, insightful visualizations of the results.

A significant aspect of this study is the comparison of our results with those obtained by Scholle *et al.* [12], which served to validate our findings. The comparative analysis highlighted the robustness of our approach and the consistency of our results with existing literature. The similarity in results confirmed the reliability of our computational framework and provided confidence in our conclusions.

Overall, this report aims to present a detailed and comprehensive analysis of magnetism in a square lattice using the Hubbard model. By integrating theoretical approximations, computational techniques, and comparative analysis, we strive to contribute valuable insights to the field of condensed matter physics. The findings of this study not only enhance our understanding of magnetic phenomena but also pave the way for future research and technological advancements in related areas.

Chapter 2

Theoretical background

2.1 Hubbard Model

The Hubbard model [4, 5, 6], independently proposed in 1963 by John Hubbard, Martin Gutzwiller, and Junjiro Kanamori, is a cornerstone theoretical framework in condensed matter physics. It is designed to explore the electronic behaviors in solids, focusing on the role of electron-electron interactions. This model is pivotal in understanding diverse and complex phenomena such as ferromagnetism, the Mott-Hubbard transition, superconductivity.

Tight-Binding Model

At the core of the Hubbard model is the tight-binding approximation, which is fundamental in describing the electronic structure of solids, particularly for materials with strong localization of electronic wavefunctions near the atomic sites. We use the tight-binding model that simplifies the complex problem of electronic motion in a crystal lattice by assuming that electrons can only "hop" between nearest neighbor sites and that the overlap of wavefunctions between more distant neighbors is negligible.

The tight-binding method, also known as the Linear Combination of Atomic Orbitals (LCAO) method, is a technique that allows the Bloch function of a periodic system to be written as a linear combination of atomic orbitals. The tight-binding approximation helps in understanding and calculating the band structure (energy levels, electronic band dispersion) of solids where electrons are likely to be localized within the nanomaterials.

Atomic Hamiltonian

The tight-binding method is described as follows [3]: First, consider the Hamiltonian of an isolated atom:

$$\hat{H}_{at} = -\frac{\hbar^2 \nabla^2}{2m_e} + V_{at}(\vec{r}) \tag{2.1}$$

where

$$\hat{H}_{at}\Phi_j = \epsilon_n^0 \Phi_j \tag{2.2}$$

Here, ∇ is the nabla operator acting on the electron coordinates, V_{at} is the single-electron potential, and $^0\epsilon_j$ is the eigenenergy of the eigenfunction ϕ_j of an isolated atom. When an atom is surrounded by other atoms within a crystal, the associated electrons feel the presence of these neighboring atoms through the potential $\Delta V(\vec{r})$, which has the same periodicity as the crystal. This potential allows the valence electrons of an atom to delocalize, having a non-zero

probability of being found in the orbitals of neighboring atoms. The term "tight-binding" refers to the fact that in $\Delta V(\vec{r})$, the electrons remain on the atomic orbitals of an isolated atom.

Crystal Hamiltonian

$\hat{H}_{sol}$ is the Hamiltonian that acts on the atomic orbital states in the solid. Combining all the different atomic energies gives the energy band structure of the crystal (solid),

$$\hat{H}_{sol} = -\frac{\hbar^2 \nabla^2}{2m_e} + \sum_{\vec{r}_i} V_{at,i}(\vec{r} - \vec{r}_i), \tag{2.3}$$

where the sum is over all positions $\vec{r}_i$ of the atomic orbitals in the crystal. The first term corresponds to the kinetic energy, and the second term is the sum of the potential energy over all the atoms in the crystal. Considering the potential $\Delta V(\vec{r})$ defined previously,

$$\hat{H}_{sol} = \hat{H}_{at} + \Delta V(\vec{r}). \tag{2.4}$$

From this equation, the wave functions of the crystal (Bloch functions) must be written as a superposition of all the atomic orbitals present in the crystal. If there are N_{orb} atomic orbitals per unit cell, we must consider N_{orb} Bloch functions:

$$\Phi_{j,\vec{k}}(\vec{r}) = \frac{1}{\sqrt{N}} \sum_{\vec{R}} C_{j,\vec{k},\vec{R}} \Phi_j(\vec{r} - \vec{R}) \tag{2.5}$$

with $j = 1, ..., N_{orb}$, and $\vec{R}$ being the Bravais lattice vectors. These atomic states Φ_j can be modified for higher energies or due to the presence of other atoms. j is an orbital index in the unit cell. In our calculations, we only consider valence and conduction orbitals, so the energy is close to the Fermi level E_F. The coefficients $C_{j,\vec{k},\vec{R}}$ are determined so that the wave function $\Phi_{j,\vec{k}}(\vec{r})$ satisfies Bloch's theorem, thus,

$$\Phi_{i,\vec{k}}(\vec{r}) = \frac{1}{\sqrt{N}} \sum_{\vec{R}} e^{i\vec{k}\cdot\vec{R}} \Phi_j(\vec{r} - \vec{R}). \tag{2.6}$$

In Dirac notation, we write $\langle \vec{r}|\Phi_{j,\vec{R}}\rangle = \Phi_j(\vec{r} - \vec{R})$ and with N_{orb} being the total number of Bloch states and $j = 1, ..., N_{orb}$,

$$|\Phi_{j,\vec{k}}(\vec{r})\rangle = \frac{1}{\sqrt{N}} \sum_{\vec{R}} e^{i\vec{k}\cdot\vec{R}} |\Phi_{j,\vec{R}}\rangle \tag{2.7}$$

where N is the total number of unit cells. Let N_{at} be the number of atoms per unit cell. In our calculations, we consider one orbital per atom and one atom per unit cell, so $N_{at} = N_{orb}$. N_{orb} is the dimension of the Hilbert space in which we work, *i.e.* the space spanned by the Bloch states $\Phi_{j,\vec{k}}(\vec{r})$, $j = 1, ..., N_{orb}$.

In our work, we assume that the basis of atomic orbitals is orthonormal,

$$\langle \Phi_{i,\vec{R}}|\Phi_{j,\vec{R}'}\rangle = \delta_{i,j}\delta_{\vec{R},\vec{R}'}. \tag{2.8}$$

According to the Schrödinger equation, we obtain the N_{orb} Bloch functions (Bloch states) $\Psi_{n,\vec{k}}(\vec{r})$ with eigenenergies $\epsilon_n(\vec{k})$:

$$\hat{H}_{sol}\Psi_{n,\vec{k}}(\vec{r}) = \epsilon_n(\vec{k})\Psi_{n,\vec{k}}(\vec{r}) \tag{2.9}$$

i.e. in Dirac notation,

$$\hat{H}_{sol}|\Psi_{n,\vec{k}}(\vec{r})\rangle = \epsilon_n(\vec{k})|\Psi_{n,\vec{k}}(\vec{r})\rangle \tag{2.10}$$

These eigenstates are calculated in the basis of $\Phi_{j,\vec{k}}$,

$$|\Psi_{n,\vec{k}}(\vec{r})\rangle = \sum_{j=1}^{N_{orb}} b_{n,\vec{k}}|\Phi_{j,\vec{k}}\rangle \tag{2.11}$$

To find the eigenstates and eigenenergies of this Hamiltonian, we multiply equation (2.10) by the conjugate of equation (2.11): $\langle\Psi_{m,\vec{k}}(\vec{r})|$

$$\langle\Psi_{m,\vec{k}}(\vec{r})|\hat{H}_{sol}|\Psi_{n,\vec{k}}(\vec{r})\rangle = \epsilon_n\langle\Psi_{m,\vec{k}}(\vec{r})|\hat{H}_{sol}|\Psi_{n,\vec{k}}(\vec{r})\rangle \tag{2.12}$$

$$\langle\Psi_{m,\vec{k}}(\vec{r})|\hat{H}_{sol}|\Psi_{n,\vec{k}}(\vec{r})\rangle = E_n\delta_{m,n} \tag{2.13}$$

$$\begin{cases} \epsilon_n(\vec{k}), & \text{if } n = m \\ 0, & \text{otherwise} \end{cases}$$

The main computation of this intership (and those made by Scholle et al.) were carried out in real space only, i.e., considering $\vec{k} = \vec{0}$. It can be generalized to a calculation in reciprocal space (The question is about how it affects, if it does, the results) by writing the same Hamiltonian in matrix form for all vectors $\vec{k}$ in reciprocal space, obtaining the following form (in the basis of $\Phi_{j,\vec{k}}$):

$$\hat{H}_{\vec{k}} = \hat{H}(\vec{k}) \tag{2.14}$$

$$\hat{H}_{\vec{k}} = \begin{pmatrix} \langle\Phi_{1,\vec{k}}(\vec{r})|\hat{H}_{sol}|\Phi_{1,\vec{k}}(\vec{r})\rangle & \cdots & \cdots \\ \cdots & \cdots & \cdots \\ \cdots & \cdots & \langle\Phi_{N_{orb},\vec{k}}(\vec{r})|\hat{H}_{sol}|\Phi_{N_{orb},\vec{k}}(\vec{r})\rangle \end{pmatrix} \tag{2.15}$$

$$\hat{H}_{\vec{k}} = \left(h_{i,j}\right)_{i,j=1,\ldots,N_{orb}} \tag{2.16}$$

$$h_{i,j} = \langle\Phi_{i,\vec{k}}(\vec{r})|\hat{H}_{sol}|\Phi_{j,\vec{k}}(\vec{r})\rangle \tag{2.17}$$

By considering all couplings between orbitals contained in the Bravais crystal lattice (with $\vec{R}$ being the Bravais lattice vectors), we can numerically calculate the matrix elements of $\hat{H}_{\vec{k}}$:

$$h_{i,j} = \sum_{\vec{R}} \langle\Phi_{i,\vec{R}}(\vec{r})|\hat{H}_{sol}|\Phi_{j,\vec{0}}(\vec{r})\rangle e^{i\vec{k}\cdot\vec{R}} \tag{2.18}$$

To simplify the calculations, we only consider the coupling terms between nearest neighbor orbitals with s orbitals (orbital quantum number $l = 0$), *i.e.*,

$$\langle\Phi_{i,\vec{R}}(\vec{r})|\hat{H}_{sol}|\Phi_{j,\vec{0}}(\vec{r})\rangle = \begin{cases} t_{i,j} = t & \text{if } \Phi_{i,\vec{R}} \text{ and } \Phi_{j,\vec{0}} \text{ are nearest neighbors} \\ 0 & \text{otherwise} \end{cases} \tag{2.19}$$

The Hamiltonian for the tight-binding model in Real space, for a single-band approximation is given by:

$$H_{\text{TB}} = -t\sum_{\langle i,j\rangle,\sigma}(c_{i\sigma}^{\dagger}c_{j\sigma} + \text{h.c.}) \tag{2.20}$$

Here, t represents the real hopping parameter, which quantifies the kinetic energy lost or gained when an electron moves between adjacent lattice sites. The sum over $\langle i, j \rangle$ indicates summation over nearest neighbors, ensuring that electron hopping is restricted to adjacent lattice sites only. The operators $c_{i\sigma}^\dagger$ and $c_{i\sigma}$ are the creation and annihilation operators that add or remove an electron of spin σ at lattice site i, respectively.

Hubbard Interaction Term

The Hubbard interaction term H_{int} introduces a fundamental aspect of electron-electron interactions at a microscopic level, specifically targeting the repulsive energy between two electrons occupying the same lattice site. It is given by:

$$H_{\text{int}} = U \sum_i n_{i\uparrow} n_{i\downarrow} \tag{2.21}$$

This term represents the on-site Coulomb repulsion and is characterized by U, the on-site interaction energy. The presence of U introduces electron correlation effects, capturing the physics of electron localization which is critical for phenomena like the Mott transition.

In this framework, $n_{i\sigma} = c_{i\sigma}^\dagger c_{i\sigma}$ is the number operator for electrons with spin σ at site i. When two electrons of opposite spins occupy the same site, the Hubbard term U quantifies the additional energy cost due to their mutual repulsion. This term is crucial for studying the competition between kinetic energy, favoring electron delocalization across the lattice, and potential energy, favoring electron localization to minimize repulsive interactions.

The significance of U varies widely across different materials and is a key parameter in determining the electronic phase of the system – whether it behaves as a metal, insulator, or exhibits magnetic order. It is particularly noted for its ability to model the transition from a metallic to an insulating state, known as the Mott transition, which occurs when the repulsive energy U dominates over the kinetic energy term t.

Despite its simplifications, such as neglecting long-range Coulomb interactions and lattice vibrations, the Hubbard model remains extensively used for exploring essential qualitative features of correlated electron systems in physics.

Filling Term

The chemical potential (μ) is a parameter that controls the number of particles in the system. It acts as an energy level that electrons must overcome to enter or leave the system. By adjusting the chemical potential, one can change the electron filling n. The summation $\sum_{i\sigma} n_{i\sigma}$ is over all lattice sites i and spin states σ (where σ can be either $\uparrow$ or $\downarrow$).

The Hamiltonian term

$$H_F = -\mu \sum_{i\sigma} n_{i\sigma} \tag{2.22}$$

is added to the Hubbard model to account for the effect of the chemical potential. It adjusts the energy of the system depending on the number of electrons present, effectively controlling the electron density. Including this term in the Hamiltonian ensures that the total electron number can be controlled via the chemical potential, which is essential for exploring different filling regimes and their corresponding physical properties within the model.

2.2 Hartree Approximation

Mean Field Approximation in the Hubbard Model

The Mean Field Approximation (MFA) is particularly useful in the Hubbard model for simplifying the treatment of electron-electron interactions. By assuming that each electron experiences an average interaction from the other electrons in the system, the many-body problem is reduced to an effective single-body problem. This approach is instrumental in studying phase transitions and magnetic properties in a simplified yet insightful manner [7, 10].

Consider the decomposition of the number operator $n_{i\sigma}$ for electrons with spin σ at lattice site i:

$$n_{i\sigma} = \langle n_{i\sigma} \rangle + (n_{i\sigma} - \langle n_{i\sigma} \rangle) = \langle n_{i\sigma} \rangle + \delta_{i\sigma} \tag{2.23}$$

where $\langle n_{i\sigma} \rangle$ is the expectation value of the number operator, and $\delta_{i\sigma}$ represents the fluctuation from this average.

By substituting into the expression for the interaction term in the Hubbard Hamiltonian, we obtain:

$$\begin{aligned}
n_{i\uparrow} n_{i\downarrow} &= (\langle n_{i\uparrow} \rangle + \delta_{i\uparrow})(\langle n_{i\downarrow} \rangle + \delta_{i\downarrow}) \\
&= \langle n_{i\uparrow} \rangle \langle n_{i\downarrow} \rangle + \langle n_{i\uparrow} \rangle \delta_{i\downarrow} + \langle n_{i\downarrow} \rangle \delta_{i\uparrow} + \delta_{i\uparrow} \delta_{i\downarrow} \\
&= \langle n_{i\uparrow} \rangle \langle n_{i\downarrow} \rangle + \delta_{i\uparrow} \delta_{i\downarrow} + \langle n_{i\uparrow} \rangle n_{i\downarrow} - \langle n_{i\uparrow} \rangle \langle n_{i\downarrow} \rangle \\
&\quad + \langle n_{i\downarrow} \rangle n_{i\uparrow} - \langle n_{i\downarrow} \rangle \langle n_{i\uparrow} \rangle
\end{aligned} \tag{2.24}$$

In the Mean Field Approximation, the terms involving fluctuations $\delta_{i\sigma}$ (highlighted in green) are often neglected under the assumption that their average contributions are small. This leads to the simplified Hartree interaction term:

$$H_{\mathrm{MFA}} = U \sum_i \left(\langle n_{i\uparrow} \rangle n_{i\downarrow} + \langle n_{i\downarrow} \rangle n_{i\uparrow} - \langle n_{i\uparrow} \rangle \langle n_{i\downarrow} \rangle \right) \tag{2.25}$$

This expression effectively reduces the complexity of the Hubbard interaction by replacing the product of operators with single-particle operator, allowing for analytical and numerical solutions that provide insights into the system's behavior, such as ferromagnetism or antiferromagnetism, under various conditions.

Limits of the Hartree approximation

It is important to note that such mean-field approximation shows the Hartree term in which the mean-field Hubbard term is only written for the z component of the spin moment. This is the most commonly applied way to examine the magnetic properties of a system. Nevertheless, the magnetic moment can be in favor of the xy-plane rather than the z-direction in the presence of the spin-orbit coupling. To include the x (y) component of the spin moment, the Fock term should be represented together with the Hartree term in the Hubbard Hamiltonian.

2.3 Hartree-Fock Approximation

The Hartree-Fock Approximation (HFA) offers a rigorous framework for studying electron systems, taking into account both the antisymmetry of the fermionic wave function and exchange interactions. This method is particularly valuable for capturing the nuances of spin-dependent phenomena and is essential for systems with significant spin-orbit coupling effects [1].

Hartree and Fock Terms

In the Hubbard model, the Hartree term typically focuses on the z-component of the spin moment. This approximation is useful for initial studies of magnetic properties:

$$H_{\text{Hartree}} = U \sum_i \langle n_{i\uparrow} \rangle n_{i\downarrow} + \langle n_{i\downarrow} \rangle n_{i\uparrow} \tag{2.26}$$

However, when considering spin-orbit coupling, the magnetic moments may align preferentially in the xy-plane. To include these components, the Fock term, which accounts for the exchange interactions, must also be incorporated:

$$H_{\text{Fock}} = -U \sum_i \langle c_{i\uparrow}^\dagger c_{i\downarrow} \rangle c_{i\downarrow}^\dagger c_{i\uparrow} + \langle c_{i\downarrow}^\dagger c_{i\uparrow} \rangle c_{i\uparrow}^\dagger c_{i\downarrow} \tag{2.27}$$

Application of Wick's Theorem

Using Wick's theorem, the interaction operators in the Hubbard Hamiltonian can be decoupled to facilitate a mean-field-like treatment but with inclusion of exchange effects. The typical decoupling process is demonstrated in the following derivation: [10]

$$
\begin{aligned}
n_{i\uparrow} n_{i\downarrow} &= c_{i\uparrow}^\dagger c_{i\uparrow} c_{i\downarrow}^\dagger c_{i\downarrow} \\
&\rightarrow \langle c_{i\downarrow}^\dagger c_{i\downarrow} \rangle c_{i\uparrow}^\dagger c_{i\uparrow} + \langle c_{i\uparrow}^\dagger c_{i\uparrow} \rangle c_{i\downarrow}^\dagger c_{i\downarrow} - \langle c_{i\uparrow}^\dagger c_{i\uparrow} \rangle \langle c_{i\downarrow}^\dagger c_{i\downarrow} \rangle \\
&\quad - \langle c_{i\downarrow}^\dagger c_{i\uparrow} \rangle c_{i\uparrow}^\dagger c_{i\downarrow} - \langle c_{i\uparrow}^\dagger c_{i\downarrow} \rangle c_{i\downarrow}^\dagger c_{i\uparrow} + \langle c_{i\uparrow}^\dagger c_{i\downarrow} \rangle \langle c_{i\downarrow}^\dagger c_{i\uparrow} \rangle \\
&= \langle n_{i\downarrow} \rangle n_{i\uparrow} + \langle n_{i\uparrow} \rangle n_{i\downarrow} - \langle n_{i\uparrow} \rangle \langle n_{i\downarrow} \rangle - \langle S_i^- \rangle S_i^+ - \langle S_i^+ \rangle S_i^- + \langle S_i^+ \rangle \langle S_i^- \rangle
\end{aligned}
$$

Total Hartree-Fock Hamiltonian

Combining all contributions, the total Hartree-Fock Hamiltonian for the Hubbard model can be expressed as:

$$H_{\text{HF}} = H_{\text{TB}} + H_{\text{Hartree}} + H_{\text{Fock}} \tag{2.28}$$

where H_{TB} represents the tight-binding or kinetic term, H_{Hartree} accounts for the direct Coulomb repulsion, and H_{Fock} includes the antisymmetric exchange interactions. This comprehensive Hamiltonian addresses both the direct and exchange interactions, providing a complete picture of electron dynamics and the resulting magnetic and electronic properties of the system.

This formulation of the Hartree-Fock Hamiltonian thus provides a powerful tool for studying correlated electron materials and their phase transitions, particularly in cases involving anisotropic magnetic properties and significant spin-orbit coupling effects.

2.4 Magnetic Order

The study of magnetism in square lattice systems is crucial for understanding the fundamental properties of various magnetic materials. This section explores various types of magnetic orders that can occur in square lattice systems. Each type of magnetic order represents a distinct arrangement of spins, which can be visualized through different panel representations [12, 2].

The various types of magnetic orders are as follows:

- **Paramagnetism**: In a paramagnetic state, spins are disordered and do not exhibit any long-range magnetic order. Thermal fluctuations cause the spins to align randomly, leading to zero net magnetization in the absence of an external magnetic field.

- **Néel Antiferromagnetism**: Néel antiferromagnetism is characterized by alternating spins in a checkerboard pattern. This type of order occurs at half-filling and intermediate to high values of U/t in the Hubbard model.

- **Spiral Order**: In a spiral order, the spins rotate progressively in a fixed plane, forming a spiral pattern across the lattice. This type of order can arise due to competing interactions that favor a non-collinear arrangement of spins.

- **Stripe Order**: Stripe order is characterized by parallel lines (stripes) of spins with alternating directions. This arrangement can occur due to interactions that favor the formation of domains with alternating magnetization.

- **Collinear Bidirectional Stripe Order**: In collinear bidirectional stripe order, spins align in stripes, but unlike the simple stripe order, the stripes themselves alternate in direction across the lattice, creating a more complex pattern.

- **Coplanar Bidirectional Stripe Order**: This order is similar to the collinear bidirectional stripe order but with an additional twist: the spins within each stripe lie in the same plane but are not collinear. Instead, they form a coplanar pattern.

- **Beat Order**: Beat order involves a modulation of the spin pattern, where the amplitude of spin alignment oscillates in a regular fashion. This can result from competing interactions leading to a complex periodic spin structure.

Visual Representation: To illustrate these magnetic orders, we can visualize them on a square lattice where each site represents a spin:

1. **Paramagnetism**: Randomly oriented spins with no visible pattern.

2. **Néel Antiferromagnetism**: Alternating up and down spins in a checkerboard pattern.

3. **Spiral Order**: Spins rotating in a fixed plane, forming a spiral across the lattice.

4. **Stripe Order**: Parallel stripes of up and down spins.

5. **Collinear Bidirectional Stripe Order**: Alternating stripes of spins, with direction alternating between stripes.

6. **Coplanar Bidirectional Stripe Order**: Stripes with spins in a coplanar, non-collinear pattern.

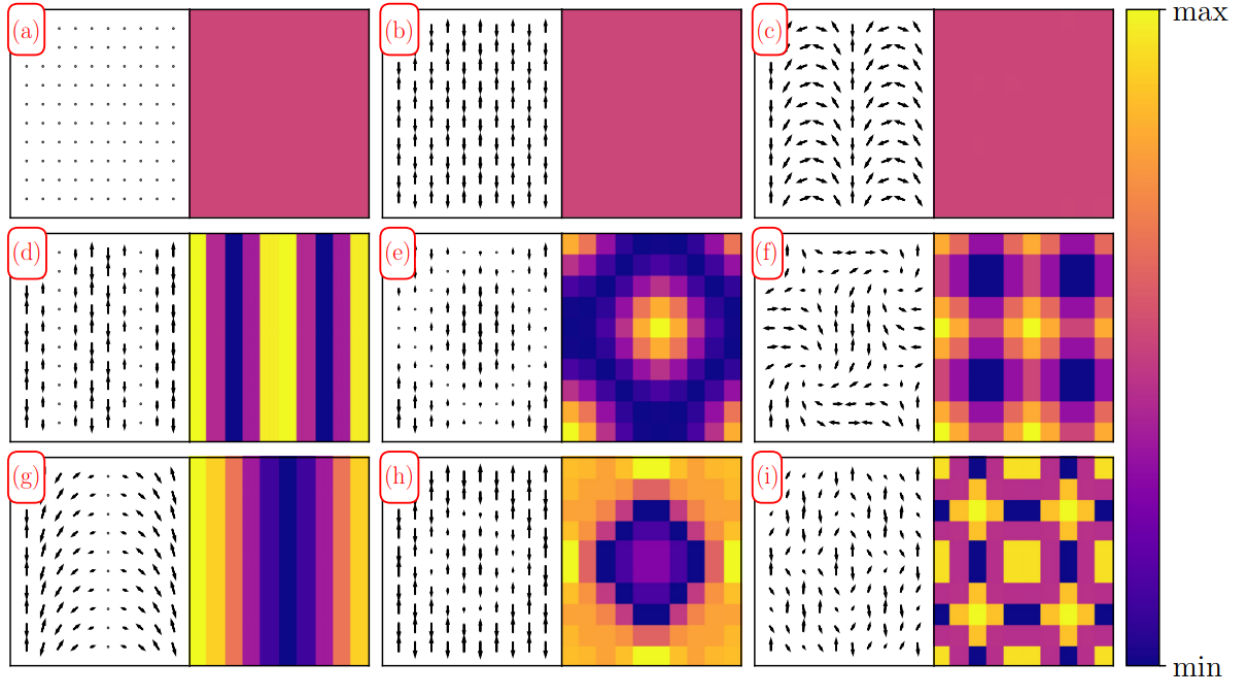7. **Beat Order**: Modulated spin alignment, forming a beating pattern.

Figure 2.1: Classification of different magnetic orders by [12]. Overview of the different orders found in their calculations, schematically shown on a 10×10 square lattice. In each panel, the square on the left shows the relative spin orientations and amplitudes (length of the arrows) of each phase, where they chose a frame such that the spins lie in the x-y plane and the bottom left spin points along the y direction. The right plot in each panel shows the corresponding charge modulation, using a color code defined on the right edge of the figure.

Chapter 3

Numerical method

This section provides an in-depth discussion of the numerical methods used to investigate the magnetic order in square lattice systems through the Hubbard model. We will cover the self-consistent algorithm, the calculation of the chemical potential, and other key computational procedures.

3.1 Computational tools

In this study, C++ and the Armadillo library were chosen for implementing the numerical methods, while Python was used for visualizing the results. Armadillo is a high-quality linear algebra library for the C++ language, providing efficient and easy-to-use functionalities for matrix operations and numerical computations. The choice of C++ over other programming languages, such as Python, is motivated by several factors.

Firstly, C++ offers superior performance and efficiency, which is crucial for handling large-scale computations and intensive numerical simulations required in this study. The compiled nature of C++ allows for faster execution times compared to interpreted languages like Python. This performance benefit is particularly important when dealing with the repeated diagonalization of large Hamiltonian matrices and extensive iterative procedures.

Armadillo, as a linear algebra library, is well-suited for scientific computing due to its intuitive syntax that closely resembles MATLAB, making it easier to write and understand code. It also provides robust support for various matrix decompositions and eigensolvers, which are essential for the diagonalization steps in the self-consistent algorithm.

For the visualization of results, Python was chosen due to its powerful libraries such as Matplotlib and Pandas. These libraries provide extensive tools for plotting and data analysis, making it easier to create detailed and informative visual representations of the computed magnetic properties. Python's simplicity and readability also facilitate quick adjustments and enhancements to the visualization code.

3.2 Self Consistent Algorithm

From a computational point of view, the diagonal elements of the Hubbard Hamiltonian matrix depend on the unknown parameters $\langle n_{i\uparrow} \rangle$ and $\langle n_{i\downarrow} \rangle$. This dependency introduces a need for a self-consistent algorithm to solve the problem, as shown in Figure 2.3. In the first step, initial values for the unknown parameters $\langle n_{i\uparrow} \rangle$ and $\langle n_{i\downarrow} \rangle$ must be provided. These initial values can be chosen randomly to ensure a good solution is found. The initial values are then plugged into the Hamiltonian matrix, and the iterative calculation begins. At each iteration cycle, the Hamiltonian matrix is diagonalized to obtain eigenvalues and eigenvectors. These eigenvalues

and eigenvectors are used to compute new spin densities, $\langle n_{i\uparrow} \rangle$ and $\langle n_{i\downarrow} \rangle$. These new spin densities serve as the initial values for the next iteration.

The procedure is repeated until the self-consistency convergence condition is satisfied. This condition is usually defined as $|A_{s+1} - A_s| < \epsilon$, where A denotes the spin densities, s is the index of the self-consistent cycle, and ϵ is a small number (typically chosen as 10^{-6}). To reach self-consistency efficiently, a linear mixing method can be employed. In this method, the spin densities for the next iteration are calculated as:

$$A_{s+1}^{\text{in}} = pA_s^{\text{out}} + (1-p)A_{s-1}^{\text{out}}$$

where p is the mixing coefficient. This approach helps to stabilize the convergence process.
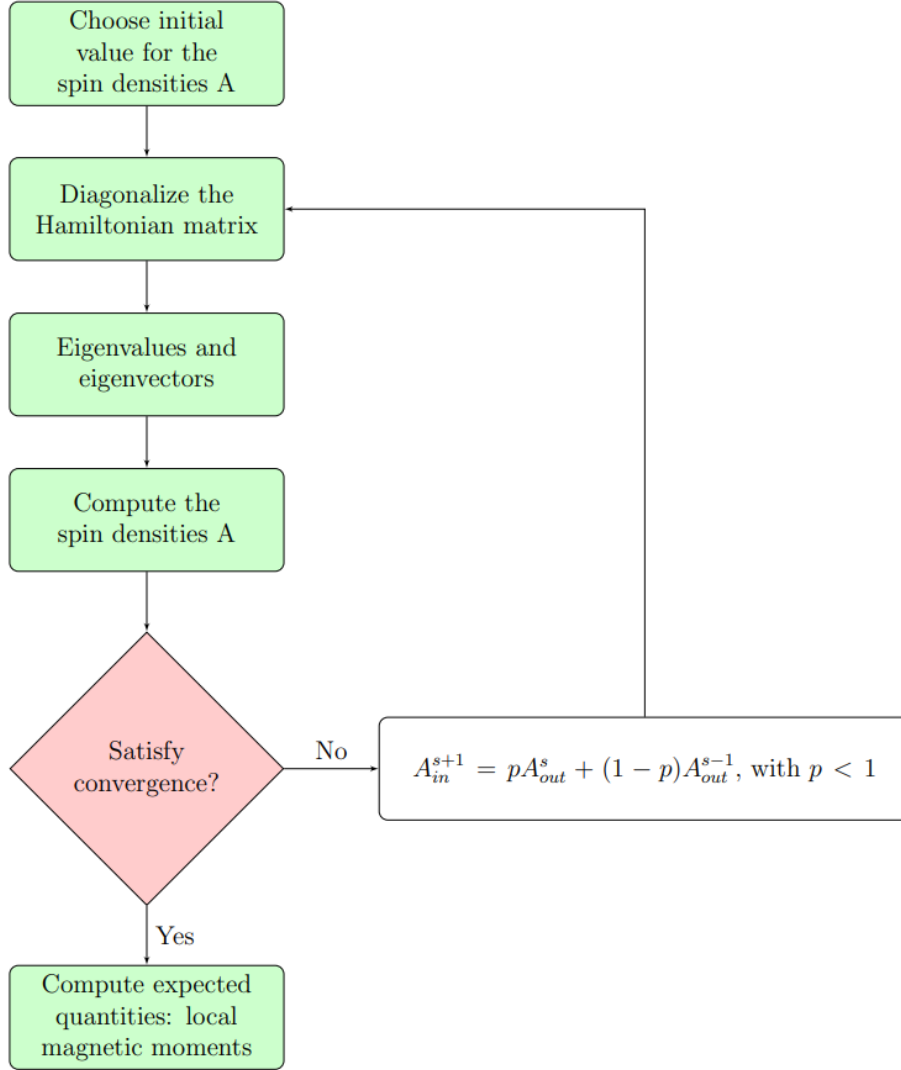

Figure 3.1: Flowchart of the self-consistent algorithm for solving the Hubbard Hamiltonian [10, 7].

At half-filling and zero temperature, the spin densities are computed from the eigenstates of the Hamiltonian [7]:

$$\Psi_n(\epsilon_n) = \sum_i^{2N} \psi_i(\epsilon_n)\Phi_i, \tag{3.1}$$

where Φ_i are the atomic orbitals (TB basis) with spin up ($\uparrow$) along z for $i = 1, ...N$ and spin

down ($\downarrow$) along z for $i = N + 1, ... 2N$. Therefore,

$$\langle n_{i\uparrow} \rangle = \sum_{\epsilon_n < E_F} \psi_i^*(\epsilon_n)\psi_i(\epsilon_n) \quad \text{and} \quad \langle n_{i\downarrow} \rangle = \sum_{\epsilon_n < E_F} \psi_{i+N}^*(\epsilon_n)\psi_{i+N}(\epsilon_n) \tag{3.2}$$

$$\langle S_i^+ \rangle = \sum_{\epsilon_n < E_F} \psi_{i+N}^*(\epsilon_n)\psi_i(\epsilon_n) \quad \text{and} \quad \langle S_i^- \rangle = \sum_{\epsilon_n < E_F} \psi_i^*(\epsilon_n)\psi_{i+N}(\epsilon_n) \tag{3.3}$$

where E_F is the Fermi energy and the ϵ_n are the eigenenergies from the diagonalisation. These equations represent the expectation values of the spin densities ($\langle n_{i\uparrow} \rangle$ and $\langle n_{i\downarrow} \rangle$) and the spin-flip operators ($\langle S_i^+ \rangle$ and $\langle S_i^- \rangle$) at site i.

When the temperature is not zero, the occupation of states is governed by the Fermi-Dirac distribution $f(\epsilon_{j\sigma})$:

$$f(\epsilon_n) = \frac{1}{e^{(\epsilon_n - \mu)/k_B T} + 1} \tag{3.4}$$

where μ is the chemical potential calculated like described in the 3.3 section. The expressions for the spin densities and spin operators become:

$$\langle n_{i\uparrow} \rangle = \sum_n f(\epsilon_n)\psi_i^*(\epsilon_n)\psi_i(\epsilon_n) \quad \text{and} \quad \langle n_{i\downarrow} \rangle = \sum_n f(\epsilon_n)\psi_{i+N}^*(\epsilon_n)\psi_{i+N}(\epsilon_n) \tag{3.5}$$

$$\langle S_i^+ \rangle = \sum_n f(\epsilon_n)\psi_{i+N}^*(\epsilon_n)\psi_i(\epsilon_n) \quad \text{and} \quad \langle S_i^- \rangle = \sum_n f(\epsilon_n)\psi_i^*(\epsilon_n)\psi_{i+N}(\epsilon_n) \tag{3.6}$$

After achieving self-consistency, we can calculate the local magnetic moments in the x, y, and z directions as follows:

$$M_i^x = \frac{\langle S_i^+ \rangle + \langle S_i^- \rangle}{2} \tag{3.7}$$

$$M_i^y = \frac{\langle S_i^+ \rangle - \langle S_i^- \rangle}{2i} \tag{3.8}$$

$$M_i^z = \frac{\langle n_{i\uparrow} \rangle - \langle n_{i\downarrow} \rangle}{2} \tag{3.9}$$

The Fermi-Dirac distribution $f(E)$ ensures that the spin densities and spin-flip operators are correctly weighted according to the thermal occupation of states, allowing for accurate computation of magnetic properties at finite temperatures.

3.3   Chemical Potential

The chemical potential is determined to ensure the correct number of electrons in the system. Two common methods for calculating the chemical potential are the bisection method and a direct iterative approach.

In the bisection method, the bounds of the chemical potential μ_1 and μ_2 are initially set at the lowest and highest eigenvalues, respectively. The method iteratively adjusts μ to balance the total number of electrons using the equation:

$$N_e = \sum_{j,\sigma} \frac{1}{1 + \exp(\beta(\epsilon_{j\sigma} - \mu))} \tag{3.10}$$

This iterative adjustment continues until the calculated number of electrons closely matches the desired number within a specified tolerance (10^8) .

Alternatively, the direct iterative approach begins with an initial guess for the chemical potential. The chemical potential μ is incrementally adjusted in small steps while recalculating the total number of electrons at each step. This process continues until the total number of electrons matches the desired electron count within a given tolerance.

1. Calculate the total number of electrons, N_e, using the current μ:

$$N_e = \sum_{j,\sigma} \frac{1}{1 + \exp(\beta(\epsilon_{j\sigma} - \mu))}$$

2. Adjust μ:

$$\mu = \mu + \Delta\mu$$

with $\Delta\mu = \frac{\max_{i,\sigma}(\epsilon_{j\sigma}) - \min_{i,\sigma}(\epsilon_{j\sigma})}{2N \times 1000}$

Chapter 4

Results and Discussion

In this section, I present the results of my study. The calculations were conducted using unrestricted real-space Hartree-Fock methods on a 6×6 lattice. Additionally, a few calculations were extended to larger lattices, with sizes up to 20×20, to ensure robustness and consistency of the findings. Periodic boundary conditions were applied throughout the study to simulate an infinite lattice by eliminating edge effects.

The hopping amplitude was set to $t = 1$, which is a standard unit of measure in such calculations, providing a reference for the energy scales involved. A moderate coupling strength of $U = 3t$ was chosen to balance the interaction effects without pushing the system into the regime where the Hartree-Fock approximation might generate spurious magnetic ordering patterns. It is well known that at strong coupling, the Hartree-Fock approximation can produce artifacts that do not accurately reflect the true physics of the system, thus those results were not considered pertinent for this discussion.

Except for a few specific cases, the temperature used in these simulations was $T = 10^{-6}$ in units of t. This effectively approximates a near-zero temperature environment, allowing for the examination of ground state properties and low-temperature behaviors without thermal fluctuations significantly influencing the results.

By conducting these calculations, we aim to gain insights into the magnetic properties and phase transitions within the square lattice under various conditions. The following sections will detail the observed magnetic states, temperature dependencies, and the effects of lattice size and boundary conditions on the system's behavior.

It is important to note that the Hubbard model employed in this study is invariant under any rotation of the set of spins in space, maintaining $SU(2)$ invariance, when using the Hartree-Fock approximation. As a result, all the presented results can be rotated by any spatial rotation without altering their physical implications. This symmetry ensures that the spin configurations and magnetic properties we observe are not biased by a specific orientation in spin space. However, if spin-orbit coupling were included in the Hamiltonian, this rotational invariance would be broken, introducing anisotropies and potentially altering the nature of the observed magnetic states and phase transitions.

4.1   Results and discussion at Half-Filling

4.1.1   Magnetic States

In the Hartree approximation

The figure 4.1 illustrates an antiferromagnetic (AFM) pattern on a 6x6 square lattice. Each lattice site is represented by a small circle, with spins depicted as arrows. The arrows alternate direction, forming a checkerboard pattern where each spin-up arrow (↑) is surrounded by spin-down arrows (↓) and vice versa. This arrangement highlights the fundamental characteristics of antiferromagnetic ordering, where neighboring spins are anti-aligned.
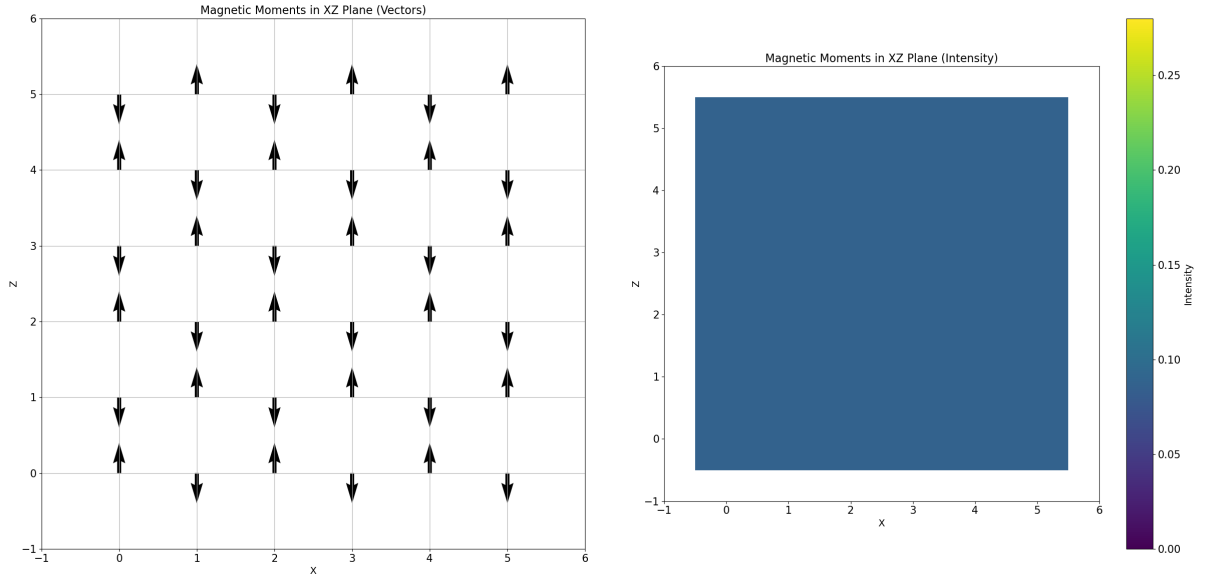

Figure 4.1: Spin configuration at half-filling on a 6×6 lattice. The left figure shows the spin projection on the xz plan. Each arrow is based on a site of the square lattice. The right figure shows the mapping of the spin amplitude in the same plant. For the antiferromagnetic state, we get an uniform picture cause all the spins, regardless the direction, have the same norm.

In terms of lattice structure, the figure displays a two-dimensional grid with equal spacing between each point, representing a simplified model of a crystalline solid. Each intersection (node) of the grid lines corresponds to a lattice site occupied by an electron. The spin configuration is visualized using arrows to indicate the direction of electron spins. Spin-up is represented by upward-pointing arrows, while spin-down is represented by downward-pointing arrows. The alternating spin configuration creates a checkerboard pattern, starting from the top-left corner with a spin-up arrow, followed by a spin-down arrow at the adjacent site to the right. This alternation continues across the row and repeats for subsequent rows, with each row beginning with the opposite spin direction of the row above.

In the Hartree-Fock approximation

With the Hartree-Fock approximation at half filling, the lattice also exhibit an antiferromagnetic pattern, but can be oriented in any direction (Figure 4.2).

The magnetic order depicted in the figure exemplifies the long-range antiferromagnetic order expected in the intermediate coupling regime ($U = 3t$ in our case) of the Hubbard model at
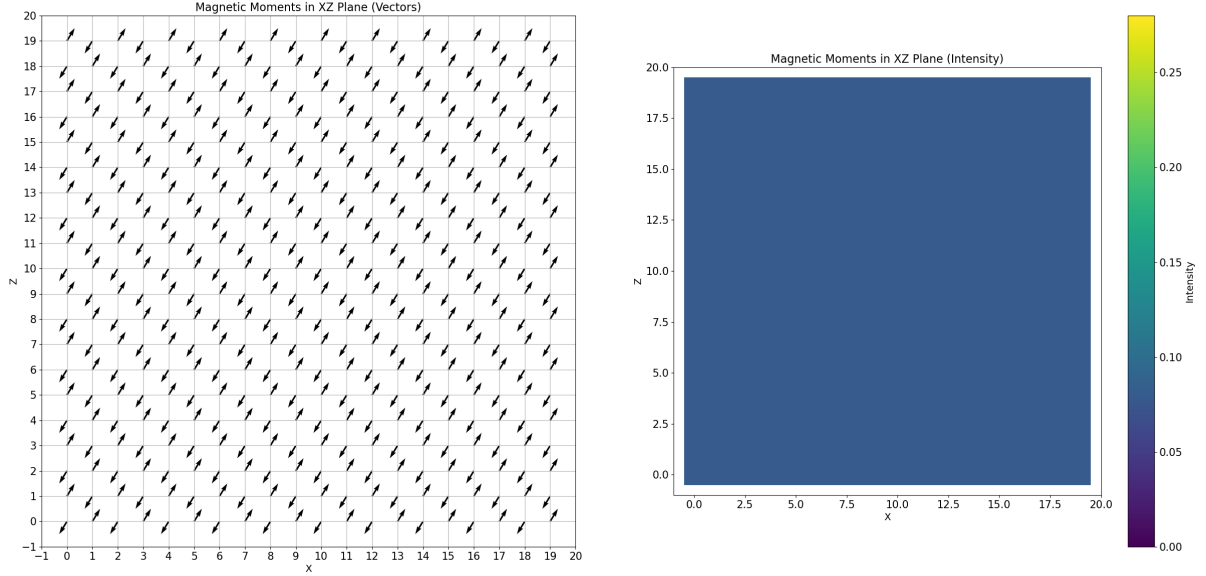
Figure 4.2: Spin projection at half-filling on a 20×20 lattice (Left) and the norm mapping in the same plan (right) .

half-filling. Each spin-up site is surrounded by spin-down sites and vice versa, minimizing the total energy of the system by reducing the likelihood of double occupancy at any site due to strong Coulomb repulsion. This pattern is a classic representation of antiferromagnetic order, where spins prefer to align anti-parallel to their nearest neighbors, minimizing the exchange energy in the system, especially in the context of the Hubbard model where on-site Coulomb repulsion is significant.

4.1.2 Temperature Dependence of Magnetic Moment

The maximum magnetic moment per site as a function of temperature is depicted in Figure 4.3. As the temperature increases, the magnetic moment decreases, indicating a transition from an ordered magnetic state to a disordered one. The point at which the magnetic moment drops significantly indicates the Néel temperature (T_N), the critical temperature above which the antiferromagnetic order is lost and the state become paramagnetic. When only considering the Hartree approximation, we can see in the figure 4.4, that bellow $T \simeq 0, 1t$, we have the apparition of three different states (characterised by different maximum magnetic moment) depending on the random distribution of the spin at the start the self consistent algorithm. This shows how difficult it is to converge to the most stable state, whereas convergence is easier in the Hartree-Fock approximation.

4.1.3 Magnetic States for an odd N

For lattices with odd N, such as 21×21, the boundary conditions prevent the formation of a perfect antiferromagnetic state. Figure 4.5 shows a non-antiferromagnetic state on a 21×21 lattice. The magnetic ordering is disrupted, leading to the formation of antiferromagnetic clusters rather than a uniform pattern. This disruption is due to the incompatibility of odd N with periodic boundary conditions, which makes it impossible to maintain a consistent antiferromagnetic order across the entire lattice. The alternation between up and down spins (periodicity of 2) is incompatible with odd periodicity. The system cannot reach it's ground state and end in a configuration with higher energy.
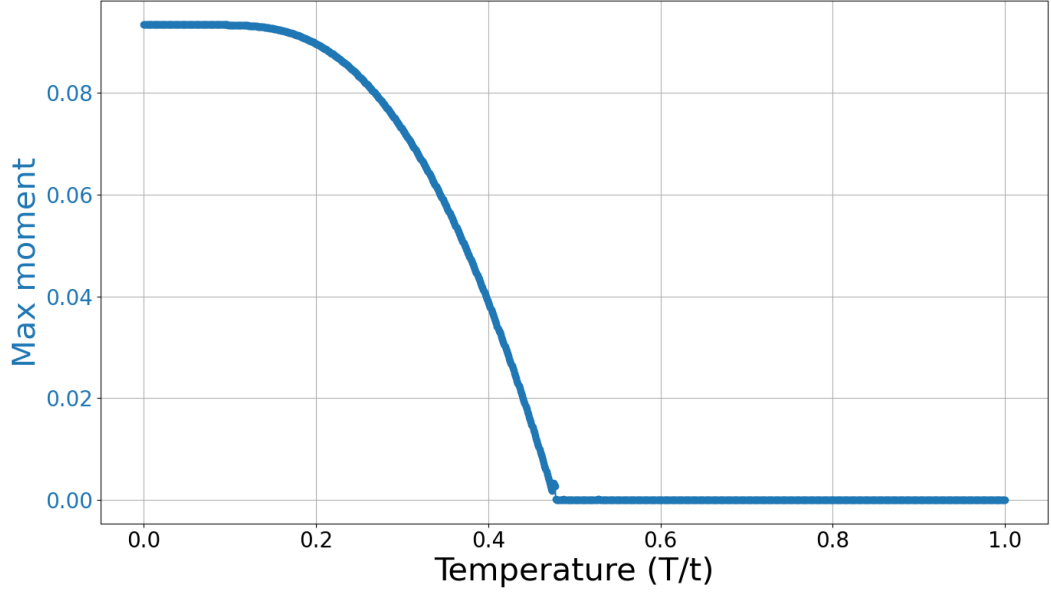
Figure 4.3: Maximum magnetic moment per site vs. temperature (in unit of t) for a 6×6 lattice at half-filling in the Hartree-Fock approximation.
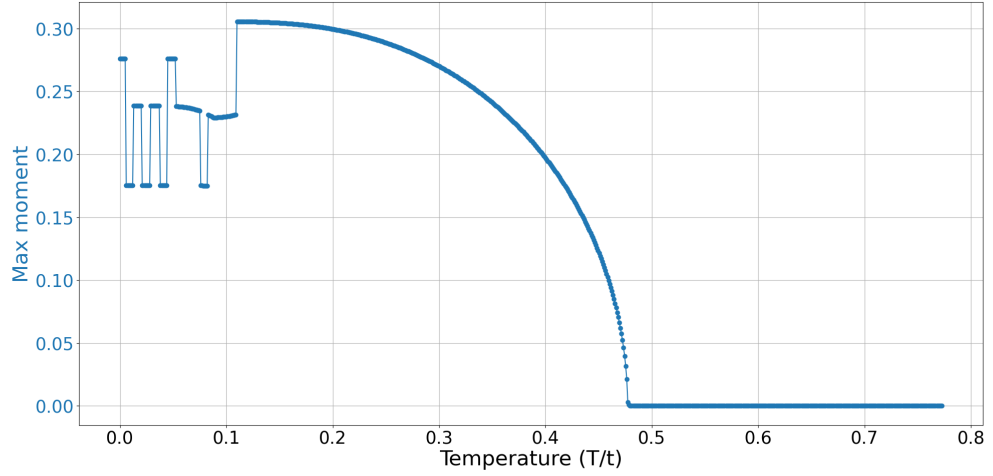

Figure 4.4: Maximum magnetic moment per site vs. temperature (in unit of t) for a 6×6 lattice at half-filling in the Hartree approximation.

4.1.4 Cluster Formation and Convergence Issues

In odd N superlattices, the formation of antiferromagnetic clusters rather than a uniform state complicates the convergence of the Hartree-Fock calculations. The presence of these clusters indicates a higher energy state compared to the ideal antiferromagnetic order, as the system struggles to minimize its energy under periodic boundary conditions. This is reflected in the difficulty of achieving convergence in the calculations, as the system oscillates between different configurations. We can see in Figure 4.6 that the odd size of superlattice require a
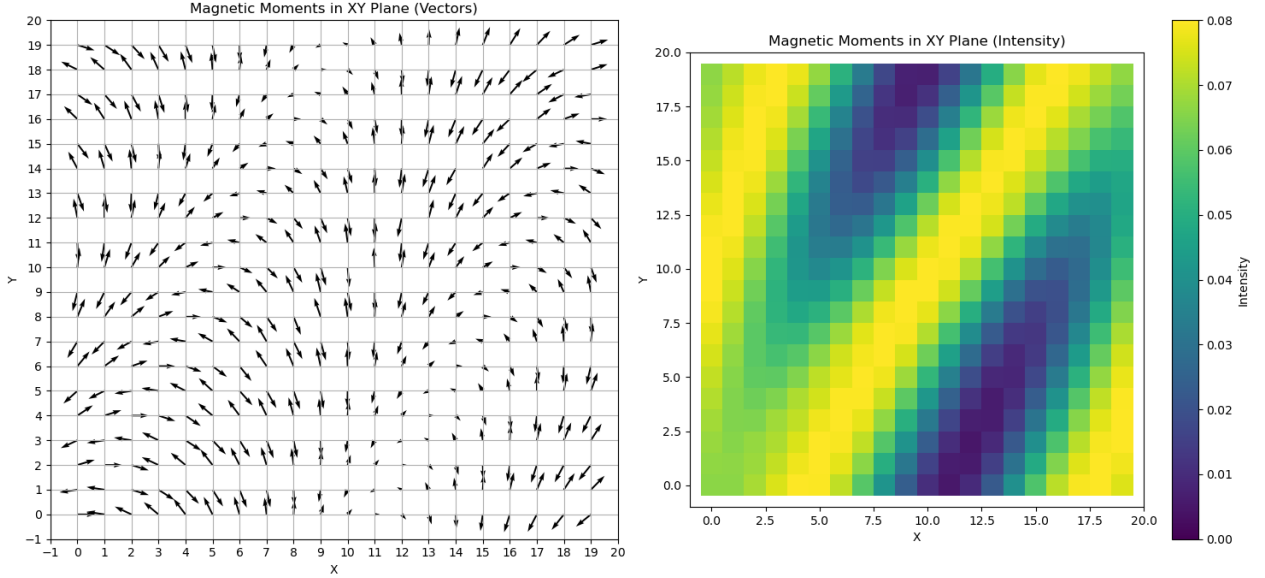
Figure 4.5: Spin configuration on odd N lattices 21×21, illustrating the disruption of anti-ferromagnetic ordering due to boundary conditions. (Left) spin projection, (right) mapping of the corresponding spin amplitude.

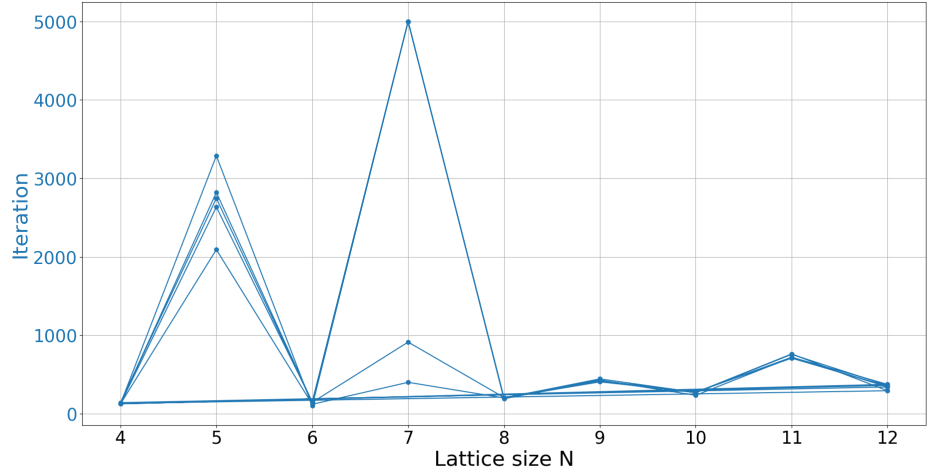higher number of iteration to achieve convergence, when it can achieve it.

Figure 4.6: Number of iteration vs size N of the supercell.

4.2 Results Bellow Half filling

4.2.1 Magnetic States

When the density (number of electron per site) goes bellow 1, we loose the perfect antiferromagnetic structure. Instead we obtain a sea of magnetic structures describe at 2.4. Our findings align with the results reported by Scholle et al. in their comprehensive mean-field
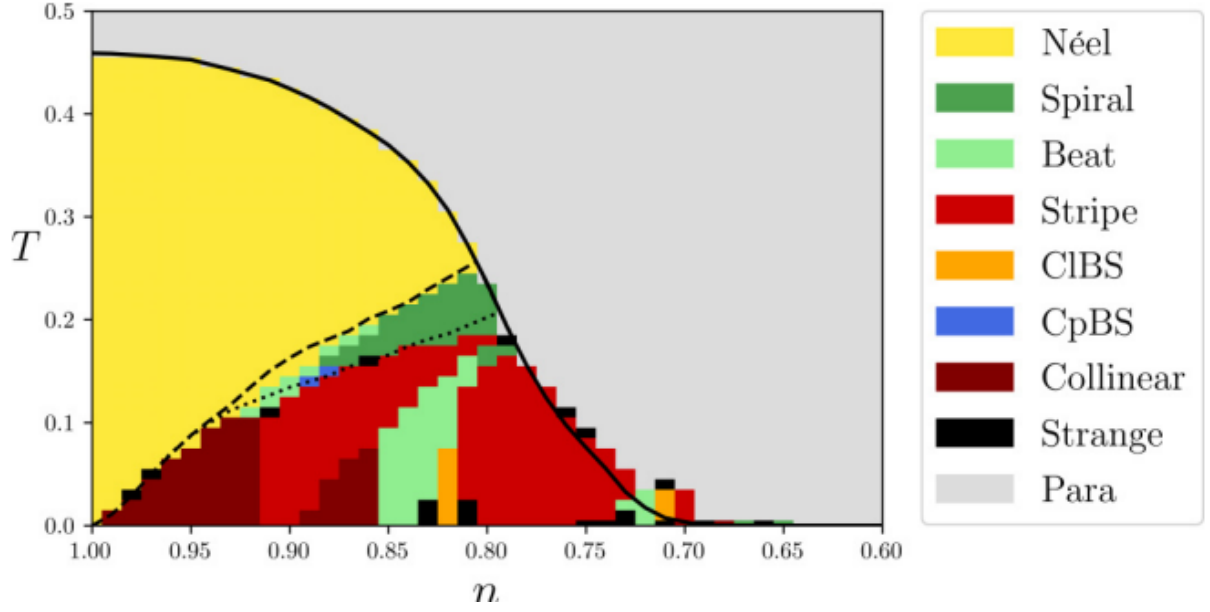
Figure 4.7: Phase diagram by [12] for $U = 3t$. The colors label the states obtained from a real-space calculation on a 20×20 lattice.

analysis of the two-dimensional Hubbard model [12]. Below half-filling and with $t' = 0$ (t' represents in their study the next-to-nearest neighbor coupling), they made a phase diagram (see 4.7 along the temperature and the density of the different magnetic states.
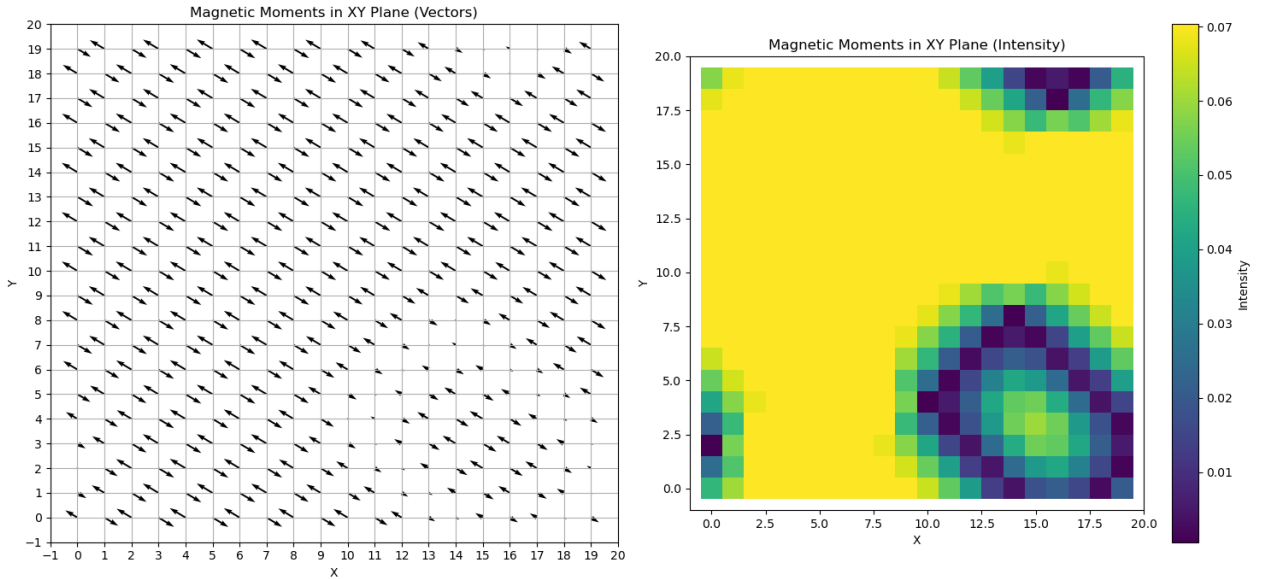

Figure 4.8: Colinear state at density $n = 0.95$ on a 20×20 lattice. (Left) spin projection, (right) mapping of the corresponding spin amplitude.

I ran calculations for a 20×20 lattice for different densities below half-filling near 0 temperature and found the Colinear state ($n = 0.95$), the Stripe state ($n = 0.90$), the Beat state ($n = 0.85$), and the Colinear Bidirectional Stripe state ($n = 0.82$).

The colinear state at density $n = 0.95$ (Figure 4.8) is characterized by spins aligning in straight, parallel lines, demonstrating a high degree of order even below half-filling. This configuration suggests a significant level of magnetic interaction that maintains this structure
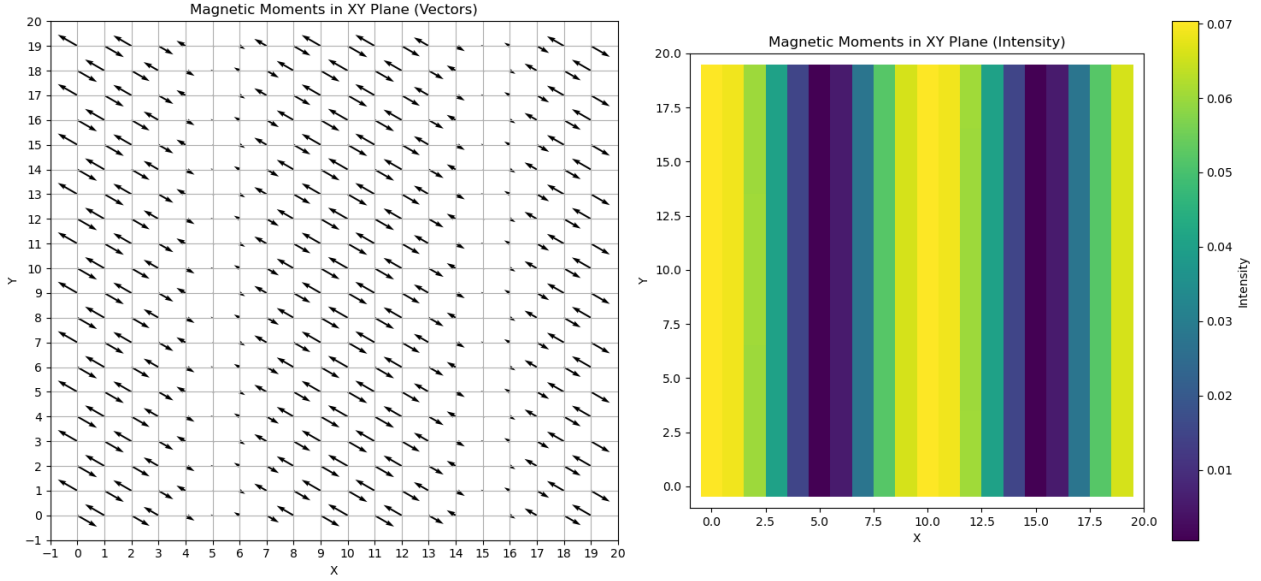
24

despite the reduction in electron density.

Figure 4.9: Stripe state at density $n = 0.90$ on a 20×20 lattice. (Left) spin projection, (right) mapping of the corresponding spin amplitude.

The stripe state at density $n = 0.90$ (Figure 4.9) shows alternating lines of up and down spins, forming a stripe pattern. This state highlights the competition between different magnetic interactions, leading to the formation of distinct domains.
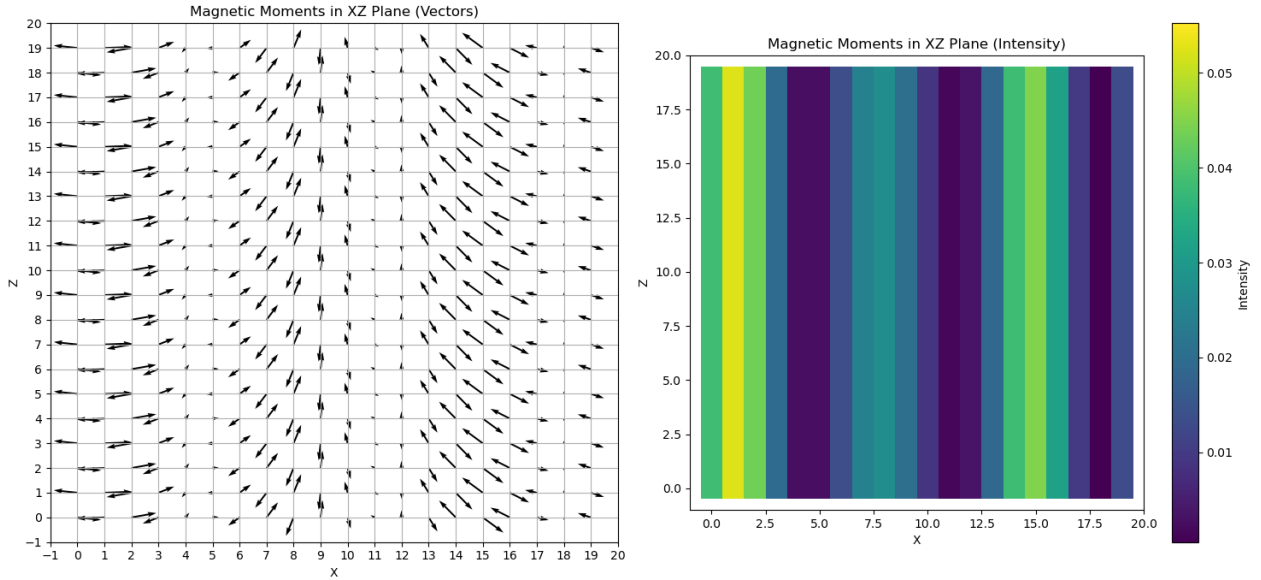

Figure 4.10: Beat state at density $n = 0.85$ on a 20×20 lattice. (Left) spin projection, (right) mapping of the corresponding spin amplitude.

The beat state at density $n = 0.85$ (Figure 4.10) features a more complex pattern, with periodic variations in the magnetic ordering. This state reflects the intricate balance of interactions that can produce non-uniform but periodic magnetic structures.

The colinear bidirectional stripe state at density $n = 0.82$ (Figure 4.11) is marked by stripes
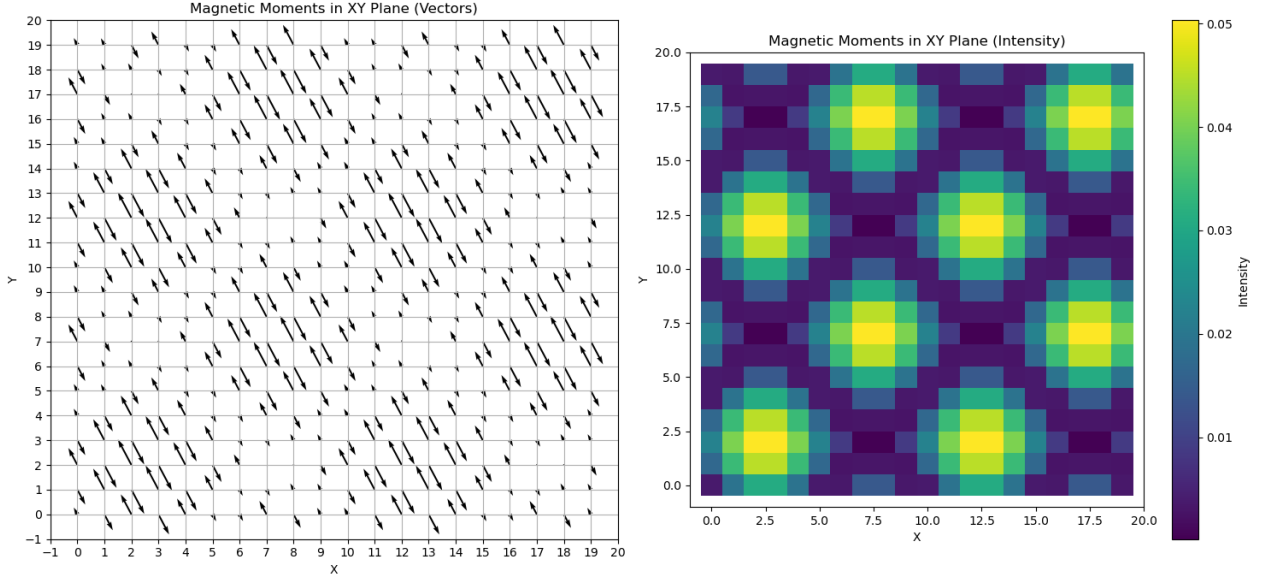
Figure 4.11: Colinear Bidirectional Stripe state at density $n = 0.82$ on a 20×20 lattice. (Left) spin projection, (right) mapping of the corresponding spin amplitude.

that not only run in parallel lines but also exhibit a bidirectional character. This indicates a more complex underlying interaction mechanism, leading to a higher level of structural complexity.

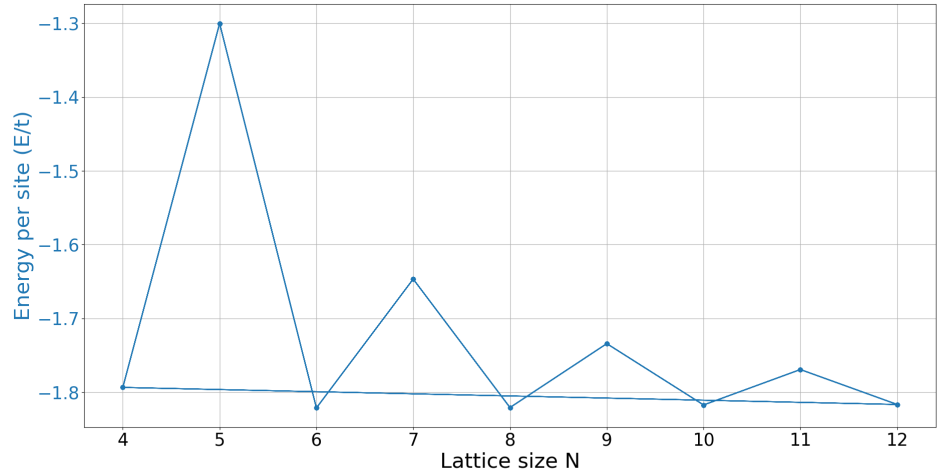### 4.2.2 Energy Per Site Analysis

Figure 4.12: Energy per site for different lattice sizes.

The energy per site for various lattice sizes and fillings is shown in Figure 4.12. At half-filling, the energy per site is lower, indicating a more stable configuration. For fillings below half, the energy increases, reflecting the frustration and higher energy configurations. This energy increase is more pronounced in odd-dimensional lattices due to the formation of anti-ferromagnetic clusters and the resultant higher energy states.
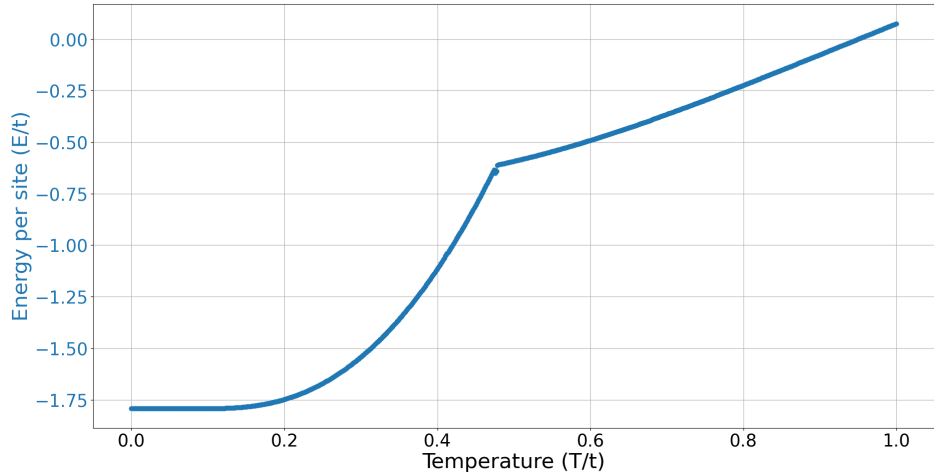
26

Figure 4.13: Energy per site vs temperature.

As the temperature increases, the energy per site shows a smooth variation. However, near the Néel temperature, a significant disruption in this behavior is observed. Specifically, the energy per site as a function of temperature exhibits a clear discontinuity in its derivative at this critical point, as illustrated in Figure 4.13. This discontinuity marks the transition from the antiferromagnetic to the paramagnetic phase, indicating the Néel temperature.

The abrupt change in the slope of the energy curve signifies a discontinuity in the heat capacity $(C_V = \left(\frac{\partial E}{\partial T}\right)_V)$ at the Néel temperature. This discontinuity in C_V is characteristic of a first-order phase transition, where the system absorbs or releases a finite amount of energy (latent heat) without a continuous change in temperature. At the Néel temperature, the long-range antiferromagnetic order is lost, and the system transitions to a paramagnetic state.

The marked change in the slope of the curve highlights the profound impact of the Néel temperature on the system's magnetic properties and serves as a hallmark of this phase transition. Above the Néel temperature, the system enters a paramagnetic state where thermal energy increases more linearly with temperature due to the random orientation of magnetic moments. This linear increase in thermal energy above T_N contrasts with the more complex behavior near the phase transition, reflecting the different magnetic interactions and orderings at play.

For a more detailed study of energy at finite temperature, the free energy of the system would have to be calculated numerically. We haven't had time to do this during this course, but it should be possible fairly easily.

4.2.3 Comparison with Previous Studies

Our findings align with the results reported by Scholle *et al.* [12] in their comprehensive mean-field analysis of the two-dimensional Hubbard model. Below half-filling and with $t' = 0$, at temperatures near zero, we observe collinear, stripe and beat order for the corresponding densities. Scholle *et al.* also identified these magnetic orders, confirming the robustness of our results and the significance of these patterns in the Hubbard model. Their detailed phase diagrams and order characterizations provide a valuable context for interpreting our data and
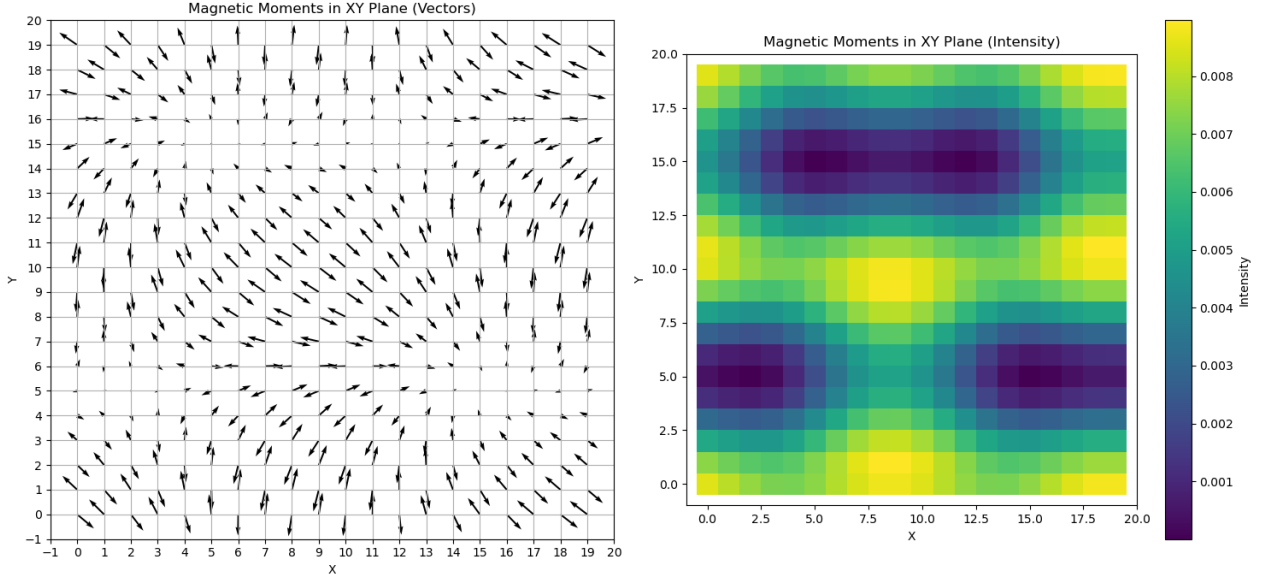
Figure 4.14: Magnetic order at $T = 0.2$, $n = 0.82$. (Left) spin projection, (right) mapping of the corresponding spin amplitude.

underscore the impact of varying coupling strengths and lattice sizes on the observed magnetic states. I also found some original states (like Figure 4.14 , that corresponds to some transition lines, in the space spanned by temperature and density.)

Chapter 5

Conclusion

This research comprehensively explores the magnetic properties of a square lattice using the Hubbard model, incorporating mean field theory and the Hartree-Fock approximation to capture the nuances of electron interactions. The primary aim was to examine magnetic order at half-filling and below, conducting simulations on lattice sizes from 6×6 to 20×20 at various temperatures.

At half-filling, our findings confirm the dominance of antiferromagnetic ordering, where spins alternate direction systematically. This consistent pattern across different lattice sizes underscores the validity and robustness of our computational approach. The study identified the Néel temperature (T_N), the critical temperature where antiferromagnetic order transitions to a disordered state, demonstrating the temperature's significant influence on magnetic properties.

Odd-dimensional lattices posed unique challenges due to periodic boundary conditions disrupting perfect antiferromagnetic order, leading to antiferromagnetic clusters and higher energy states. These conditions complicated the convergence of Hartree-Fock calculations, reflecting the inherent complexities in these systems.

Below half-filling, we discovered various magnetic states, including collinear, stripe, beat, and collinear bidirectional stripe patterns. These findings align with the phase diagrams reported by Scholle *et al.* [12], confirming the presence of diverse magnetic orders influenced by electron density. This analysis provides insights into the complex interplay between electron interactions and magnetic properties within the Hubbard model.

Energy per site analysis supported these observations, showing more stable configurations at half-filling and higher energy states below half-filling. The energy variations with temperature highlighted the impact of the Néel temperature, marking the transition from ordered to disordered magnetic states.

Our results, when compared with previous studies, particularly those by Scholle et al., validate the reliability of our computational framework and methods. The consistency of our findings with established literature underscores the robustness and significance of our approach in the field of condensed matter physics.

To further improve the accuracy of our results, future work will involve the integration over the Brillouin zone using k-point sampling. This approach will provide a more precise depiction of the electronic structure and its influence on magnetic properties. Preliminary calculations are currently underway, and we anticipate presenting these enhanced results soon. This integration

is expected to refine our understanding of the complex dynamics within the Hubbard model, offering even more robust and comprehensive insights into the magnetic behavior of square lattices.

In summary, this study offers a detailed examination of magnetism in a square lattice, enhancing our understanding of magnetic phenomena and electron interactions. By integrating theoretical approximations, computational techniques, and comparative analysis, we provide valuable insights that pave the way for future research and technological advancements in related areas. The findings not only deepen our knowledge of magnetic properties in lattice structures but also contribute broadly to condensed matter physics, with potential applications across various technological domains.

Bibliography

[1] N. W. Ashcroft and N. D. Mermin. *Solid state physics*. Holt, Rinehart and Winston, New York, NY, 1976.

[2] M. Authors. *Magnetic Order in Low-Dimensional Systems*. Springer, 2023.

[3] G. T. de Laissardière. Tight binding course. `trambly.u-cergy.fr/`, 2024. Lecture Notes.

[4] J. Hubbard. Electron correlations in narrow energy bands. *Proceedings of the Royal Society of London. Series A. Mathematical and Physical Sciences*, 276(1365):238–257, 1963.

[5] J. Hubbard. Electron correlations in narrow energy bands ii. the degenerate band case. *Proceedings of the Royal Society of London. Series A. Mathematical and Physical Sciences*, 277(1369):237–259, 1964.

[6] J. Hubbard. Electron correlations in narrow energy bands iii. an improved solution. *Proceedings of the Royal Society of London. Series A. Mathematical and Physical Sciences*, 281(1386):401–419, 1965.

[7] S. Krompiewski. Edge magnetism of finite graphene-like nanoribbons in the presence of intrinsic spin–orbit interaction and perpendicular electric field. *Nanotechnology*, 27(31):315201, jun 2016.

[8] Laboratoire de Physique Théorique et Modélisation. Laboratoire de physique théorique et modélisation. `https://lptm.cyu.fr/`, 2024. Accessed: 2024-06-20.

[9] C. D. N. MANICKA. Stage à l'université de cergy pontoise. `https://github.com/DiehlNM/Stage_cy`, 2024. Accessed: 2024-06-30.

[10] T. Phung. *Numerical studies of magnetism and transport properties in graphene nanodevices*. Theses, Université de Cergy Pontoise, Dec. 2019.

[11] C. Sanderson and R. Curtin. Armadillo: a template-based c++ library for linear algebra. *Journal of Open Source Software*, 1(2):26, 2016.

[12] R. Scholle, P. M. Bonetti, D. Vilardi, and W. Metzner. Comprehensive mean-field analysis of magnetic and charge orders in the two-dimensional hubbard model. *Physical Review B*, 108(3), 2023.

Appendix A

Main algorithm

A.1 Header

A.2 Source

Appendix B

Output

B.1 Spin plotting

B.2 Curb plotting

Appendix C

Data

C.1   Save moment

C.2   Plot moment